Available online at www.sciencedirect.com
ScienceDirect
International Journal of Heat and Mass Transfer 50 (2007) 654–666
International Journal of HEAT and MASS TRANSFER
www.elsevier.com/locate/ijhmt

A benchmark solidification experiment on an Sn–10%wtBi alloy

G. Quillet, A. Ciobanas, P. Lehmann, Y. Fautrelle *

EPM laboratory, CNRS/INPG/UJF, ENSHMG BP 95, 38402 Saint Martin d'Hères cedex, France

Received 9 March 2005; received in revised form 20 October 2005
Available online 21 November 2006

Abstract

The solidification of a 90/10%wt tin–bismuth alloy has been analyzed experimentally for a 50 × 60 × 10 mm ingot. The heat flux was extracted from one vertical side of the ingot. Instantaneous temperature measurements were performed using a lattice of 25 thermocouples located on one of the large sides of the sample. The temperature versus time curve exhibits the classical pseudo-plateau as well the eutectic step. A post-mortem analysis of the samples was carried out. Solidification is almost columnar over the range of solidification rates considered. Two types of segregations are observed. X-ray analysis reveals the development of segregated channels near the cold wall. Analysis of the solute composition shows the existence of significant macro-segregations. The locations of the segregations are confirmed by the measurements of the eutectic fraction.

Keywords: Solidification; Metallic alloys; Benchmark experiment

1. Introduction

In the processing of solute rich alloys, defects called macro-segregations can result from the solidification step. They are characterized by composition differences within the dimensional scale of the product, deteriorating the properties of the material. In most cases, such defects are observed on macrographs of the product. Besides large scale macro-segregation, one particularly striking form is the "channel segregate". Typical dimensions are several cm in length and a few millimeters in cross section, representing "freckles" or chimneys on transverse sections. Such defects are observed in different solidification processes (e.g. forge ingots, vacuum-arc remelted ingots and directionally solidified turbine blades). They typically occur for relatively slow solidification rates in alloys having a relatively large solidification interval (nickel-based alloys [1], high alloy steels [2,3], Pb–Sn alloys [4] and ammonium chloride solutions for laboratory studies [4,5]). Some specific thermo-solutal convection configurations in the solid–liquid mush are also known to produce such channel segregates [3,6–9].

Various laboratory-scale solidification experiments have already been performed. The case of a pure metal was investigated by Gau and Viskanta [10]. Regarding the solidification of alloys, a reference experiment was carried out by Hebditsch and Hunt [11]. It consisted in solidifying a rectangular vertical ingot and demonstrated the appearance of solute macro-segregation related to natural convection. Sarazin and Hellawell [7] investigated the solidification of a vertical cylindrical Pb–Sn rod. The cooling rate was a few Kelvins per minute. Channel segregates were observed both on the side and inside of the ingot. Similar experiments with the same type of alloy and geometry have been carried out by Tewari and Shah [9] and Bergman et al. [12]. Macro-segregation in the solidified ingot was observed as well as channel segregates for a sufficient cooling rate, typically 2–5 K min^{-1}.

The aim of the present study was to carry out a well instrumented experiment, suitable for the validation of numerical models. The present benchmark is a solidification experiment where the cooling temperature gradient is perpendicular to the gravity. Such a configuration promotes

* Corresponding author. Fax: +33 476 82 5249.
E-mail address: Yves.Fautrelle@inpg.fr (Y. Fautrelle).

0017-9310/$ - see front matter © 2006 Elsevier Ltd. All rights reserved.
doi:10.1016/j.ijheatmasstransfer.2006.07.030

natural convection and therefore macro-segregations. We have focused our measurements on the temperature field and on segregation analysis, both on the meso-scale and macro-scale. The apparatus is described in Section 2. The pure tin case is considered in Section 3 in order to validate the temperature measurements. Section 4 is devoted to the solidification of the tin–bismuth alloy. Some concluding remarks are made in Section 5.

2. Apparatus and measurement procedures

A quasi-two-dimensional geometry was used to facilitate comparison of experimental and numerical results. Various experiments were performed. First, pure tin was used in order to calibrate the different parts of the experimental system, especially the temperature measurements. Secondly, a tin–wt.10%bismuth alloy was investigated to obtain solidification data on a well-known alloy. The overall aim was twofold:

(i) to determine the instantaneous temperature distribution during solidification,
(ii) to carry out a post-mortem analysis of the solute segregations and metallographic structures.

2.1. General principle

The general principle used to implement the experiment is sketched in Fig. 1. The ingot consists of a parallelepiped with the dimensions indicated in Fig. 2 and weighing 0.227 kg. The dimensions were based on the results of a numerical study showing that such a configuration allows the formation of segregations (see Ref. [1] for example). The sample is placed inside a stainless steel crucible, chosen as thin as possible (0.5 mm) in order to minimize its thermal inertia. The ingot is cooled laterally on one vertical side by a water-cooled copper part used as a heat exchanger. The heat losses are minimized on the other sides of the ingot by the use of a Kirchhoff box and a rarefied atmosphere. Temperature measurements are performed by a lattice of thermocouples welded to the stainless steel crucible using a silver based alloy. A post-mortem analysis of the segregations is carried out after each experiment. The different parts of the facility are described and explained below.

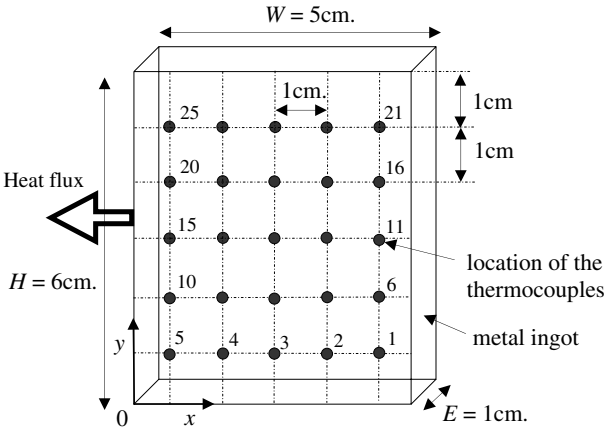

Fig. 2. Sketch of the ingot and location of the lateral thermocouples.

A special quenching facility was designed to prepare ingots satisfying two requirements: (1) homogeneity of the alloy in the ingots after preparation and (2) easy reproducibility of ingot preparation. The alloy which is presently is tin with 10%wt bismuth. The phase diagram of such an alloy is shown in Fig. A.1 of Appendix A, whilst its physical properties are provided in the same annex. The purity of the metals used is 99.99 wt.%.

2.2. The copper heat exchanger

As already mentioned, the alloy is melted or solidified by means of a copper part placed on the left side of the ingot. This piece has three zones (cf. Fig. 2):

- a cold left-end zone that is cooled by a water circulation system to extract heat during the solidification process;

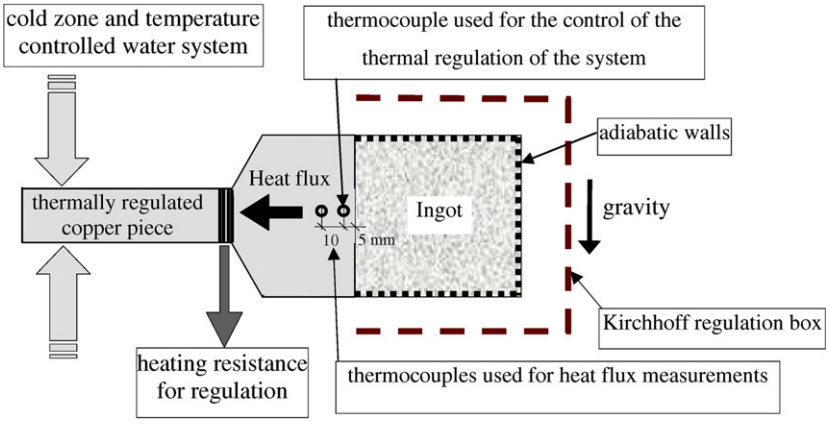

Fig. 1. General view of the solidification experiment.

- a hot middle zone with a heating element that allows different heating or freezing possibilities. The heating element is controlled by a PID system linked to a number of thermocouples located on the right end of the copper heat exchanger. Such a configuration allows us to control the melting or solidification process (ramp, Heavyside function, fixed temperature, etc.);
- a right-end zone, made up of a copper parallelepiped, used to control the temperature and heat flux on the left side of the ingot via thermocouples located within the copper block (at mid-thickness as shown in Fig. 1). One of the thermocouples (the nearest to the heat exchanger – ingot interface) controls the heating element via a PID system. The other thermocouples check the temperature at the interface by extrapolation and are used to determine the extracted heat flux.

2.3. Boundary conditions for the ingot

The ingot is thermally insulated except on one side where the heat flux is extracted as indicated in Fig. 1. The cooling system imposes a linear decay of the temperature in the copper cooler near the ingot. Adiabatic conditions are obtained by a combination of means. First, to avoid heat losses by conduction and convection, the solidification system (the steel crucible and copper heat exchanger) is placed inside a vacuum enclosure where the pressure is set to 10^{-5} atmosphere. Secondly, the thermal radiation of the ingot is minimized by placing the ingot inside a thermally regulated copper Kirchhoff box (cf. Fig. 1). In this way radiation losses are reduced to an acceptable rate. The resulting equilibrium between absorption and emission allows us to consider the crucible to be adiabatic.

2.4. Temperature measurement system

Temperature maps are recorded versus time during the solidification process via a lattice of 25 thermocouples located on one of the large side walls as shown in Fig. 2. Special attention is paid to several connections on the measurement channel in order to avoid parasitic currents (such as Seebeck effect). Indeed, any parasitic thermal gradient on a connection creates an additional electric current (called the Seebeck current) which distorts the results. In order to avoid this, all connections are contained in a controlled temperature box. The relative accuracy of the temperature measurement is approximately ± 0.1 K. However, an offset value could still be present in the temperature measurement. Such an offset was corrected thanks to a calibration achieved by means of the solidification/melting experiments of pure tin. Since the exact melting temperature of this metal is known, it can be linked to the measured melt temperatures. The remaining uncertainty regarding the absolute value of the temperature is of order of 1 K. All measurements are recorded in ASCII files via a computer. The typical time step of the sampling process is one second. We checked the reproducibility of the temperature measurements by comparing the temperature data for two identical experiments (e.g. corresponding to samples no. 5 and 6 in Fig. 11). The temperature differences between the two experiments were less than 1 K.

The extracted heat flux Φ was calculated using the temperature measurements made by thermocouples located in the copper part (see Fig. 1). The value of Φ is estimated from the temperature gradient as follows:

$$\Phi \approx C_{\mathrm{th}}\Delta T \quad \text{with the thermal conductance } C_{\mathrm{th}} = \frac{\lambda_{\mathrm{Cu}} S}{d} \approx 23.2\ \mathrm{W/K} \tag{1}$$

where λ_{Cu} ($\lambda_{\mathrm{Cu}} = 386$ W/m/K), ΔT, d and S respectively denote the thermal conductivity of copper, the temperature difference between the two thermocouples located in the copper part (cf. Fig. 1), their spacing ($d = 10$ mm) and the contact surface area between the ingot and the copper part. From (1), the uncertainty of the heat flux is related to that of the temperature by

$$\delta\Phi/\Phi \approx 2\delta T/\Delta T \tag{2}$$

Owing to the high value of the thermal conductance C_{th}, the value of the temperature difference between the two thermocouples in the copper is quite weak. For example considering a heat flux of order of 10 W (see Fig. 10 for example) yields a value of $\Delta T \approx 0.4$ K. The relative uncertainty $\delta\Phi/\Phi$ which is then of order of 50%, is quite high. The value $\delta\Phi$ is almost of the same order as the heat flux itself. As a consequence, when the temperature fluctuations are important, significant heat flux fluctuations are observed as well. For example in the case of the alloy the temperature fluctuations recorded by the heat exchanger thermocouple (Fig. 6a) are larger than those recorded in the case of pure tin (Fig. 3a). This leads to stronger heat flux fluctuations for the alloy case as shown by the comparison between Figs. 5 and 10. The above estimate indicates also that in the copper heat exchanger the temperature variations along the main direction of the heat flux are quite small. Accordingly, even though the temperature in the copper piece along the cooled boundary is likely not rigorously constant, its transverse variations (perpendicular to the heat flux direction) are smaller. This may be interpreted by the fact that the thermal diffusion time τ_{Cu} in the copper along the mid-height which is estimated by

$$\tau_{\mathrm{Cu}} \approx \frac{H^2}{\alpha_{\mathrm{Cu}}} \tag{3}$$

is equal to 32 s, α_{Cu} being the copper thermal diffusivity ($\alpha_{\mathrm{Cu}} = 1.1 \times 10^{-4}\ \mathrm{m^2/s}$) and H the sample height. The value of τ_{Cu} is small compared with the solidification time. Note that the diffusion time across the thickness of the heat exchanger is much smaller (less than 1 s). A numerical calculation of the heat transfer in the heat exchanger and the sample at solid state [13] (aimed at designing the particular shape of the copper piece in Fig. 1) showed that the

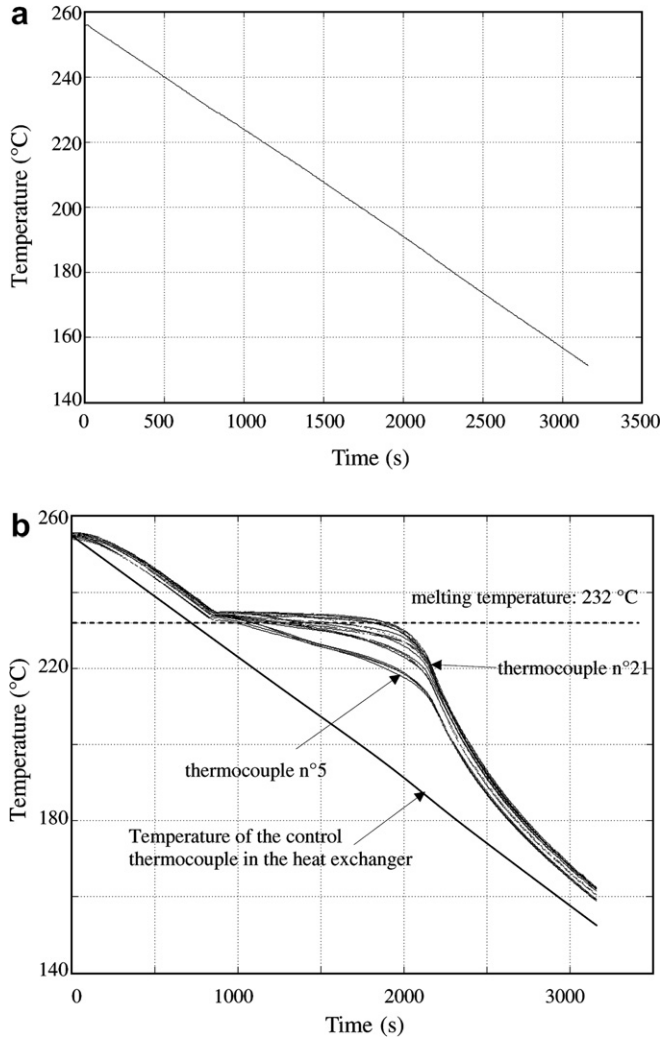

Fig. 3. Solidification of a pure tin ingot. The cooling rate is -2 K min^{-1}. The time origin corresponds to the beginning of the cooling. The initial temperature is $T_i = 255$ °C: (a) instantaneous value of the temperature in the copper heat exchanger used to regulate the cooling and (b) temperature versus time at various locations of the ingot.

transverse temperature variations along the sample boundary did not exceed 0.3 K. In conclusions the temperature of the control thermocouple is close to the copper temperature along the cooling wall with an estimated error of ± 0.3 K. In the tin sample the thermal diffusion time is higher ($\alpha_{Sn} = 3.4 \times 10^{-5}$ m^2/s), and accordingly the temperature variations along the cooled wall are expected to be higher, what was observed in the experiments.

Thanks to the lattice of temperature measurements, it is also possible to deduce the instantaneous volume-average temperature $\overline{T}(t)$ defined as follows:

$$\overline{T}(t) = \frac{1}{V}\int_V T\,\mathrm{d}v \approx \frac{1}{N}\sum_{i=1}^{N=25} T_i(t), \tag{4}$$

where V, N and $T_i(t)$ respectively denote the volume of the sample, the number of thermocouples and the instantaneous recorded values of the temperature.

Knowledge of $\overline{T}(t)$ may be used to determine the heat flux as well as the released latent heat. Assuming adiabatic conditions on the boundaries of the sample, the integration of the heat equation in a volume coinciding with the sample yields the following relation:

$$\int_V \rho c_p \frac{\partial T}{\partial t}\,\mathrm{d}v \approx m c_{\mathrm{pl}} \frac{\mathrm{d}\overline{T}}{\mathrm{d}t} \equiv \Phi_S = \Phi + L\frac{\mathrm{d}m'}{\mathrm{d}t}, \tag{5}$$

L, m and m' respectively being the latent heat and the mass of the sample and the solid phase. Concerning the estimate of the left-hand side term of Eq. (5), the heat capacity has been supposed constant. The value c_{pl} of the pure liquid tin at its melting point has been used to estimate the integral (see its value in Table A.1 of Appendix A). Indeed, the heat capacity jump between solid and liquid at the melting point is equal to 6% of the liquid value c_{pl}. The value of Φ_S may be interpreted as a term describing the heat accumulation in the ingot. Note that without any phase change, relation (5) is a second way to estimate the extracted heat flux Φ, and the values of Φ and Φ_S should be identical.

2.5. Post-mortem analysis of the samples

A qualitative pattern for the segregations has been obtained post-mortem by X-ray analysis. The bismuth easily absorbs the X-rays, and the gray-color contrast gives some indication of the solute distribution within the ingot. Bismuth-rich solute zone are easily visible and appears in white in the photography. Such a non-destructive method yields an overall view of the solute concentration segregations across the depth of the ingot, especially those that are localized, i.e. the segregated channels. Proportioning by dissolution was carried out on one ingot to obtain a map of bismuth concentration. Mapping of macrostructures and the eutectic fraction were also performed in order to study the position of channels within the ingot.

2.6. Experimental procedure

The experimental procedure used to solidify the ingot is the following:

Step 1: the ingot is heated and melted until a temperature of 250–255 °C is reached on the control thermocouple located in the heat exchanger near the sample (see Fig. 1),

Step 2: the temperature of the copper heat exchanger is maintained at the same value during 30 min approximately in order to stabilize thermally the ingot and to homogenize both the temperature and the solute in the case of the alloy,

Step 3: the temperature of the heat exchanger is imposed to decay with a constant cooling rate at $t = 0$ (-2 K min^{-1} or -5 K min^{-1}). The time evolution of the temperature provided by the control thermocouple is shown in Figs. 3a, 6a, and 7a.

3. Pure metal: experimental results

The first series of experiments were performed with pure tin in order to calibrate the experiment on the basis of fusion/solidification cycles without any segregations. We will present here the results of the solidification experiments. Details on the melting phase may be found in a PhD thesis by Quillet [13].

In the solidification experiment, the initial liquid temperature is fixed at 255 °C with less than 1° between the maximum and minimum value measured temperature during the stabilisation process which lasts 30 min approximately. Then the temperature of the control thermocouple in the copper heat exchanger is imposed to decrease linearly at $t = 0$ s (see Fig. 3a). The time evolution of the temperature measured by the 25 thermocouples are shown in Fig. 3b. In the beginning of the cooling of the liquid sample the temperatures decay slowly with respect to the copper wall. The slope of the temperature curves tends to the same cooling rate (-2 K min^{-1}) until the beginning of the solidification ($t \approx 800$ s) only after a transient of 100 s approximately. The latter transient time could be mainly linked to the time required for the establishment of the temperature field as well as the natural convection in the sample. The transient involves both the thermal and viscous diffusions. A crude estimate can obtained from the thermal diffusion time across the whole ingot such that

$$\tau_{Sn} \approx \frac{W^2}{\alpha_{Sn}} = 72 \text{ s}.$$

The latter time is not contradictory with the observations. At $t = 800$ s the value of the difference is approximately equal to 5 K, whilst the measured extracted heat flux (cf. Fig. 5) is equal to 3.5 W. The value of the corresponding heat transfer coefficient is $h \approx 1170$ W/m^2/K. Note that as expected the contact resistance is higher when the sample is solidified. For example at the end of the solidification the temperature difference is approximately equal to 10 K as shown in Fig. 3b. Note also that the temperature at the beginning of the plateau in Fig. 3b is close to the melting temperature of pure tin. This confirms that the absolute error of the temperature values is smaller than 1 K.

The instantaneous temperature maps are shown in Fig. 4 for three times. At $t = 800$ s (beginning of solidification), the isotherm corresponding to the melting temperature indicates that the bottom part of the fluid near the solidification front is the coolest zone. The temperature values are provided in Appendix B. This could correspond to a downward flow along the front. Similar results have been observed both in experiments and numerical calculations [13]. However, at $t = 1250$ s, the isotherm patterns are quite different. The global pool temperature stops decreasing because of the latent heat release which is not extracted efficiently. The downward flow transports the latent heat near the bottom region of the ingot, what could explain the curvature of the liquidus isotherm becomes negative. This is confirmed by the change of the extracted heat flux

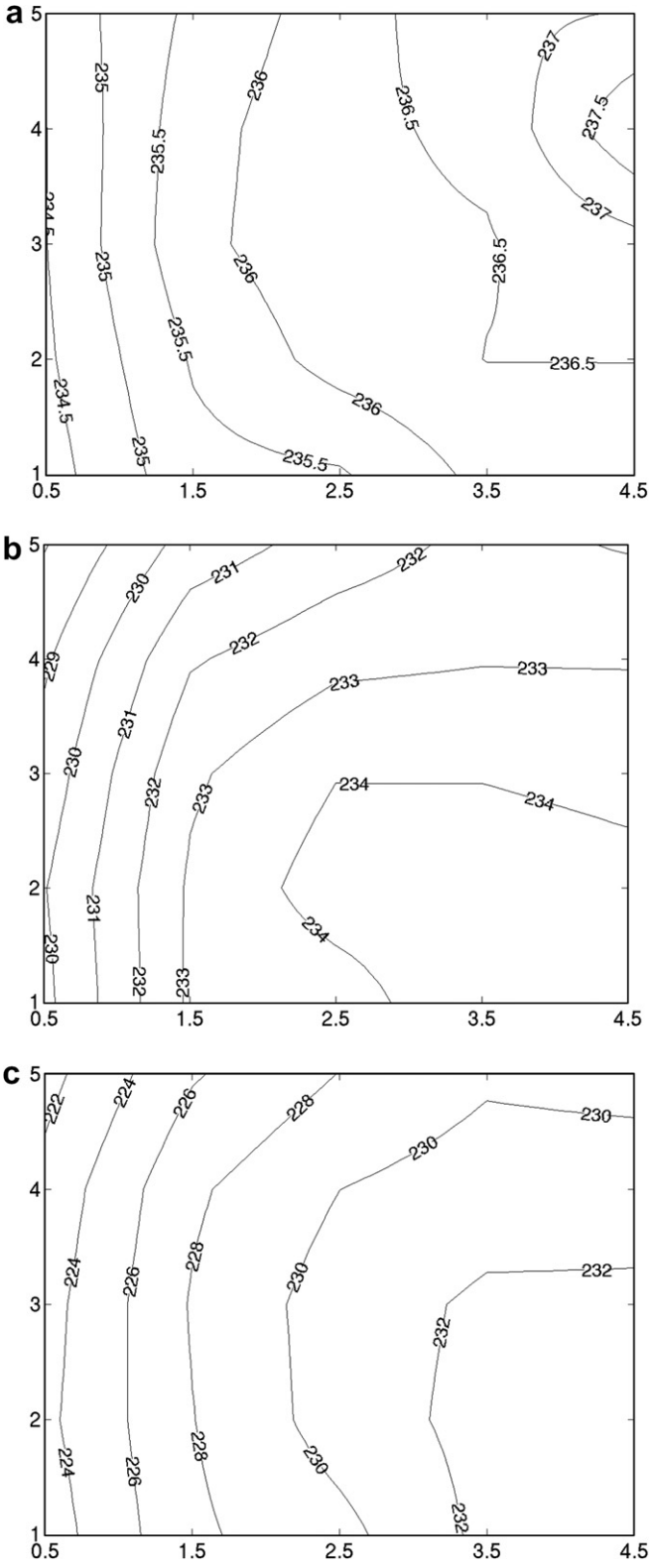

Fig. 4. Instantaneous temperature maps in the pure tin case; cooling rate -2 K min^{-1}; (a) $t = 800$ s [$T_{min} = 234.289$ °C; $T_{max} = 237.033$ °C]; (b) $t = 1000$ s [$T_{min} = 231.19$ °C; $T_{max} = 234.673$ °C]; (c) $t = 1750$ s [$T_{min} = 221.339$ °C; $T_{max} = 233.298$ °C].

Φ_S with time as shown in Fig. 5. Thus the cooling system extracts only the latent heat during the first part of the

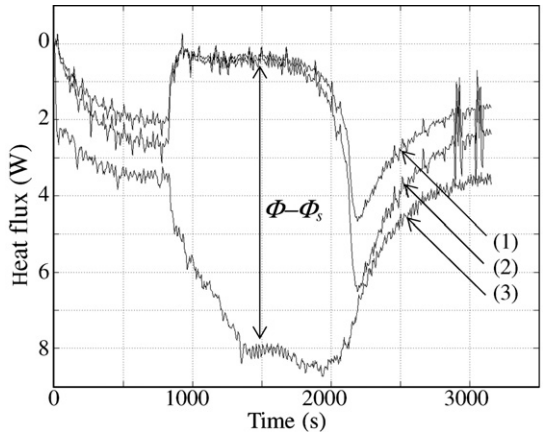

Fig. 5. Heat flux measurements in the pure tin case; cooling rate $-2\ \mathrm{K\ min^{-1}}$; (1) time evolution of the total heat stored in the sample corresponding to Φ_s in Eq. (5) and (2) time evolution of Φ_s corrected by the presence of the crucible; (3) time evolution of the extracted heat flux Φ measured from the thermocouples located in the cooling system. According to (4) the difference $\Phi - \Phi_s$ indicates the latent heat release.

solidification. Note that there is a significant discrepancy between Φ and Φ_S before the triggering of the solidification. The discrepancy is reduced if we correct the value of Φ_S by using in Eq. (5) an effective capacitance which takes into account the thermal inertia of the crucible as well. The effective capacitance is then defined as follows:

$$mc = mc_{pl} + m_c c_{pc},$$

m_c and c_{pc} respectively being the mass and the heat capacity of the stainless steel crucible. Nevertheless the remaining discrepancy may a direct consequence of the high value of the thermal conductance of the copper cooler, and the heat flux difference is consistent with the error estimate (2). From Fig. 5, the heat flux $\Phi - \Phi_S$ corresponding to the released latent heat is of the order of 8 W. That value is consistent with the following simple estimate deduced from Eq. (5):

$$\Phi - \Phi_S = L\frac{dm'}{dt} \approx L\frac{m}{t_s}, \tag{6}$$

t_s being a typical solidification time. If we consider that an order of magnitude t_s may be deduced from the time above which all the pool temperature is below the melting temperature we obtain from Fig. 3 an estimate of $t_s \approx 1800$ s. According to the above relation, $\Phi - \Phi_s$ is estimated to be 7.3 W.

4. Binary alloy: experimental results

The experimental results consist of temperature field recordings as well as some segregation pictures from post-mortem analyses of the ingot. The experimental procedure is analogous to that used in the previous pure tin case. The initial liquid temperature is fixed at 250 °C with less than 1° between the maximum and minimum value measured temperature during the stabilisation process. Then the temperature of the control thermocouple in the copper heat exchanger is imposed to decrease linearly at $t = 0$ s (see Figs. 6a and 7a). Some data on the physical properties of tin are presented in Table A.1 of Appendix A.

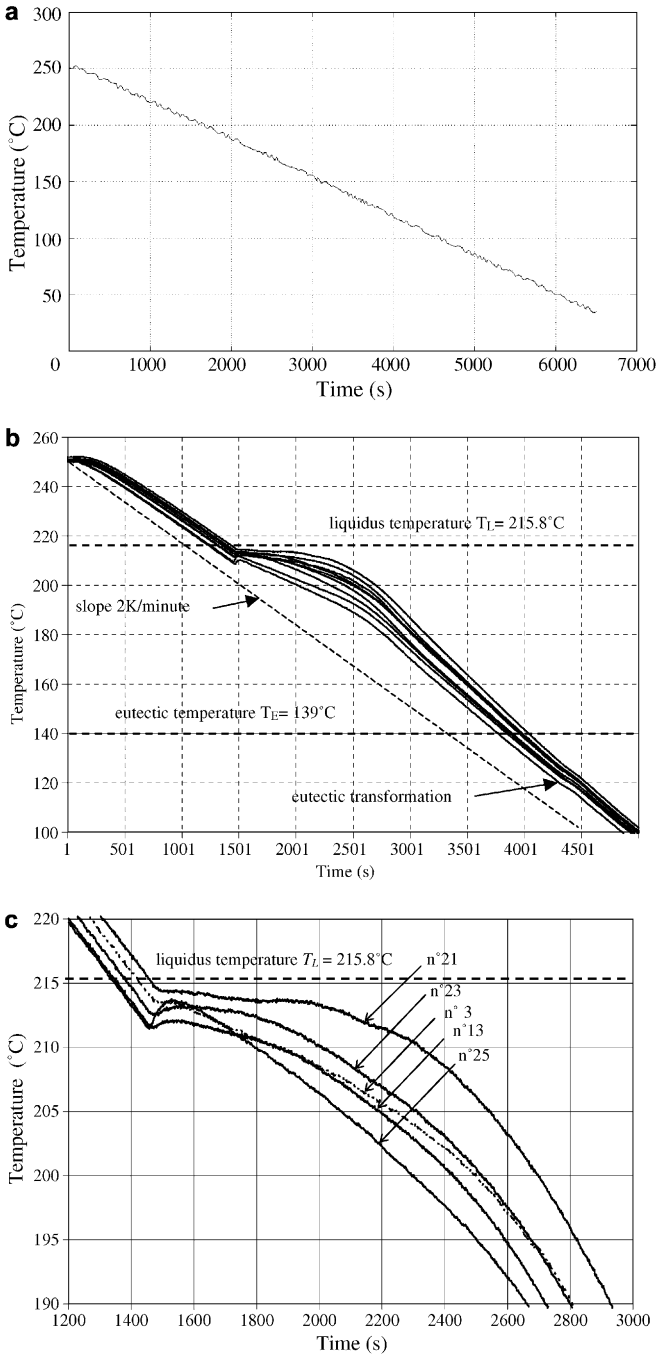

Fig. 6. Temperature curves during the solidification of Sn–wt10%Bi ingot; cooling slope: $-2\ \mathrm{K\ min^{-1}}$. The time origin corresponds to the beginning of the cooling. The initial temperature is $T_i = 250$°C: (a) instantaneous value of the temperature in the copper heat exchanger used to regulate the cooling; (b) overall view; (c) magnified view near the pseudo-plateau.

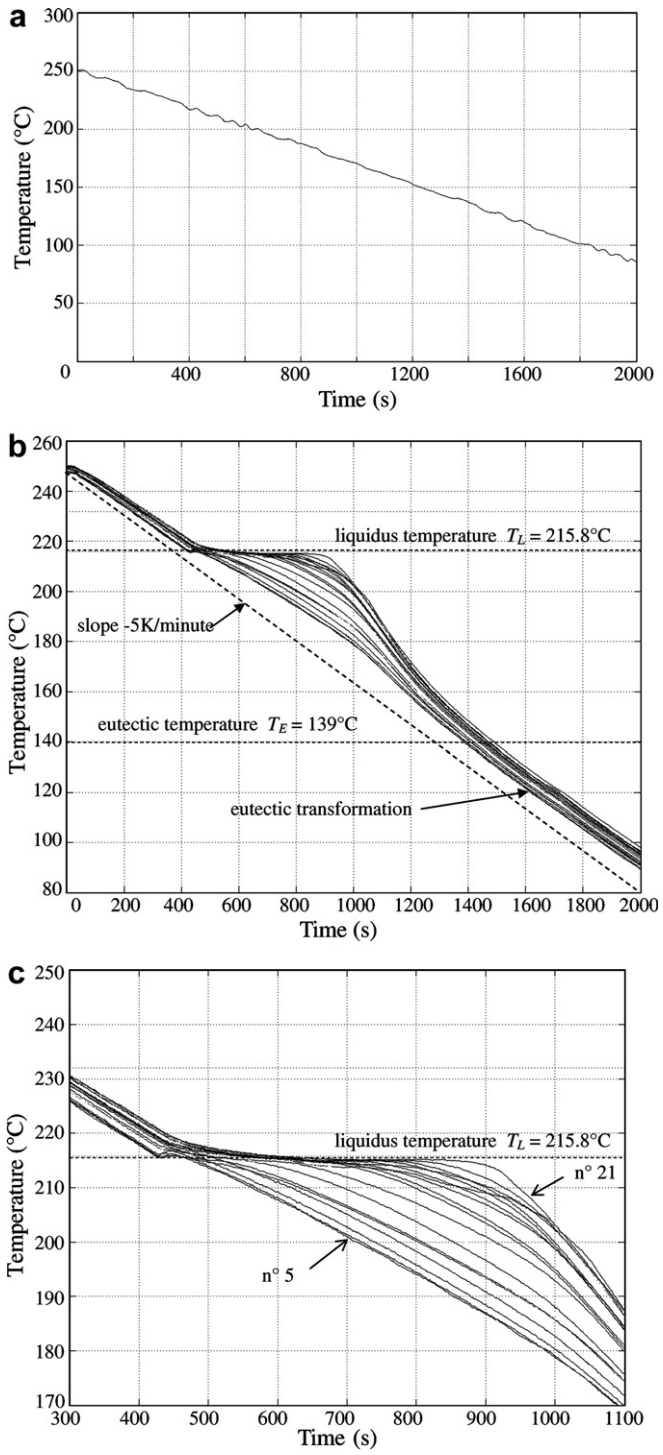

Fig. 7. Temperature curves during the solidification of Sn–wt10%Bi ingot; cooling slope: -5 K min^{-1}. The time origin corresponds to the beginning of the cooling. The initial temperature is $T_i = 250$ °C: (a) instantaneous value of the temperature in the copper heat exchanger used to regulate the cooling. (b) overall view; (c) magnified view near the pseudo-plateau.

4.1. Temperature measurements

4.1.1. Temperature maps

The recordings of the temperature versus time are shown in Figs. 6 and 7 for two cooling rates, namely -2 K min^{-1} and -5 K min^{-1}. For a cooling rate of -2 K min^{-1}, a significant undercooling (almost 4 K) occurs before the triggering of solidification (see for example Fig. 6b). It is noticeable that the above effect was observed in all the repeated experiments which were carried out. This phenomenon has not been fully explained. Various reasons might explain the temperature difference. The first reason could be linked to the measurements themselves, since it was not possible to fully master the offset value (of order of 1 K) on the thermocouples. Secondly, a physical reason could also explain the fact that the observed temperature are significantly below the liquidus temperature. Indeed, it is noteworthy that the latter effect is more pronounced in the case of the slower cooling rate. A possible interpretation lies on the fact that for the slow cooling rate case the overall solute rejection is likely higher since the convective flow has time enough to transport the solute from the mushy zone to the liquid bulk. This is confirmed qualitatively by the X-ray pictures of Fig. 11, where the segregations seem to be more important in the slow cooling case. Accordingly, the local solute enrichment could slow down the solidification due to the lowering of the liquidus temperature.

A smooth recalescence phenomenon may be observed, especially near the upper part of the cold wall (thermocouple number 25). This is likely due to the latent heat release in the sample. It is also likely that once the solidification begin, the decrease of the thermal contact between the ingot and the copper piece already observed in the previous case (Section 3) slows down the latent heat release and emphasize the recalescence. This is confirmed by the fact that the temperature increase is much weaker when the extracted heat flux is higher (-5 K min^{-1}). For the case with 5 K min^{-1} cooling (e.g. Fig. 7), the temperature curves are much closer to the liquidus temperature, and the pseudo-recalescence is less pronounced. This pseudo-recalescence is not due to a possible appearance of equiaxed grains, since on one hand the temperature increase seems to be quite slow and on the other hand the solidified structures (shown in Section 4.4) are not equiaxed.

Concerning the time evolution of the temperature a weak slope change is observed near the eutectic temperature both in Figs. 6 and 7. However, this slope change occurs unexpectedly at a temperature which is significantly lower than the eutectic temperature (10 K approximately). A possible explanation could be related to an underestimate of the temperatures due to the decrease of the thermal contact between the solid sample and the crucible.

From the local temperature recordings, it is possible to reconstruct the instantaneous maps of the temperature field at a given time (see the detailed values in Appendix C). Figs. 8 and 9 show the isotherm maps for two solidification velocities and different times. Note that the isotherms are bent near the cold wall. This is likely a consequence of the natural convection. Indeed, the cold-fluid motion near the front is oriented downward and creates a concave solidification front as sketched in Fig. 11.

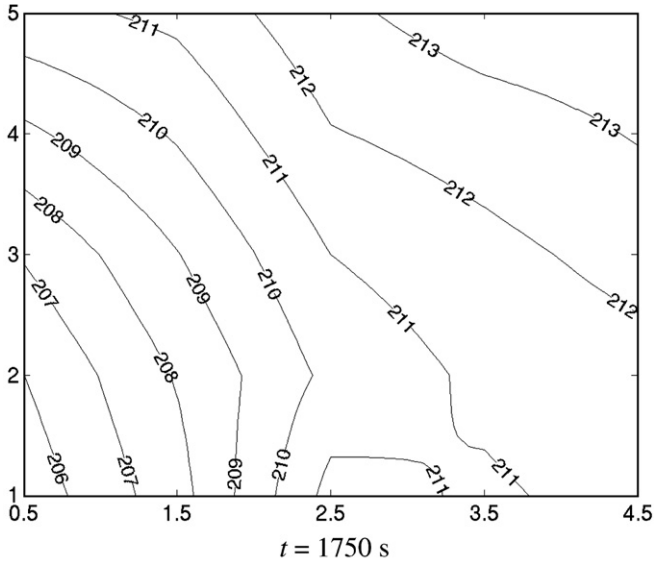

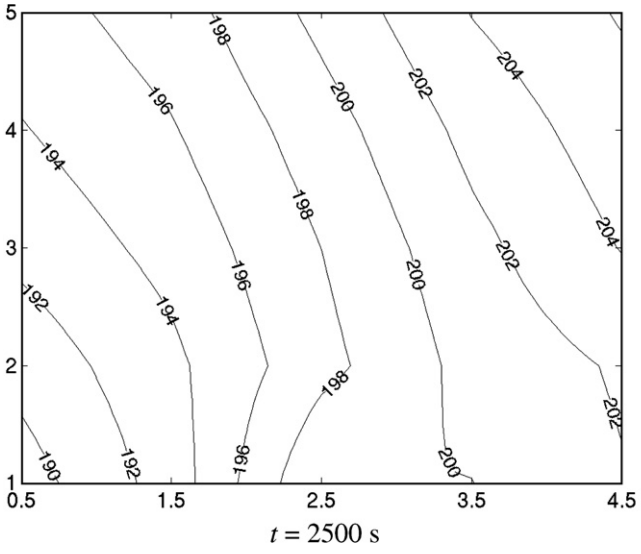

Fig. 8. Instantaneous temperature maps for the tin–bismuth case; cooling rate: -2 K min^{-1}.

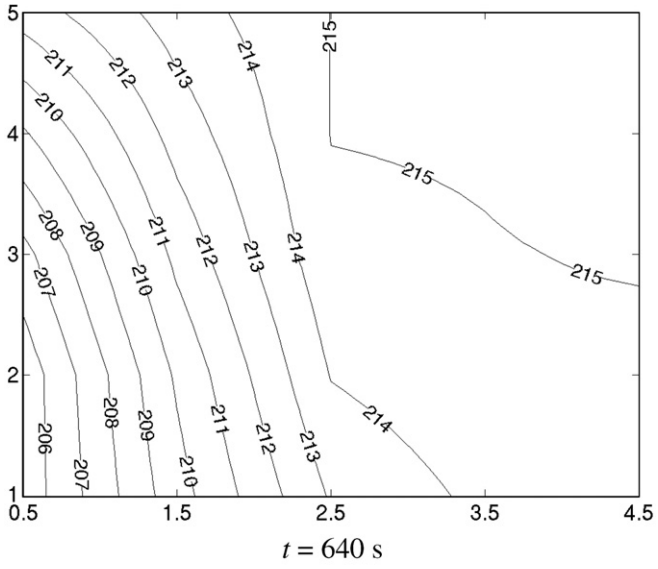

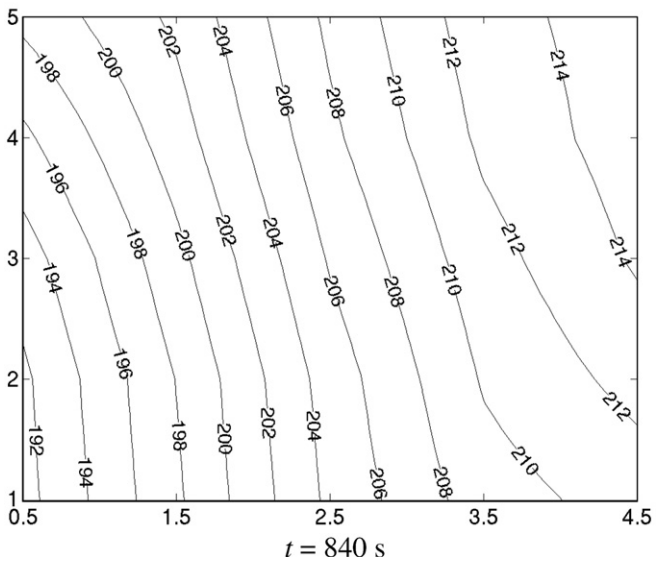

Fig. 9. Instantaneous temperature maps for the tin–bismuth case; cooling rate: -5 K min^{-1}.

4.1.2. Heat flux measurement

The extracted heat flux versus time is shown in Fig. 10. Note that the fluctuations are much greater than for the pure tin case. They may be explained by the fact that any temperature fluctuation on the control thermocouple leads to strong heat flux variations (cf. Section 2.4). It may be noticed that in opposition to the pure tin case the control thermocouple exhibits in the case of alloy significant temperature fluctuations as shown in Figs. 6a and 7a. This could be consistent with the greater fluctuations of the bath temperature also observed in the alloy (cf. [13]), however this cannot be totally affirmed since spectral analysis of the bath temperature fluctuations reveals a peak at a frequency of 0.8 Hz [13], i.e. significantly higher than the frequencies of the heat flux fluctuations. Note however that the heat exchanger filters out the rapid fluctuations because of the thermal skin effect, making it difficult to compare characteristic frequencies. Furthermore, temperature fluctuations are still observable below the eutectic temperature, what makes the interpretation difficult.

4.2. X-ray analyses

As for the solute segregations, the results obtained by X-ray analysis are illustrated in Fig. 11. The white zones observed correspond to regions enriched with bismuth. Two types of segregations may be distinguished: concentrated stripes, the channel segregates, in the left part of the ingot (Fig. 11b and c for example) and large diffuse regions located in the bottom right part (Fig. 11a for example). It is not possible to make a clear distinction between the two cooling rates. The segregation patterns are qualitatively similar, although it seems that the segregations are

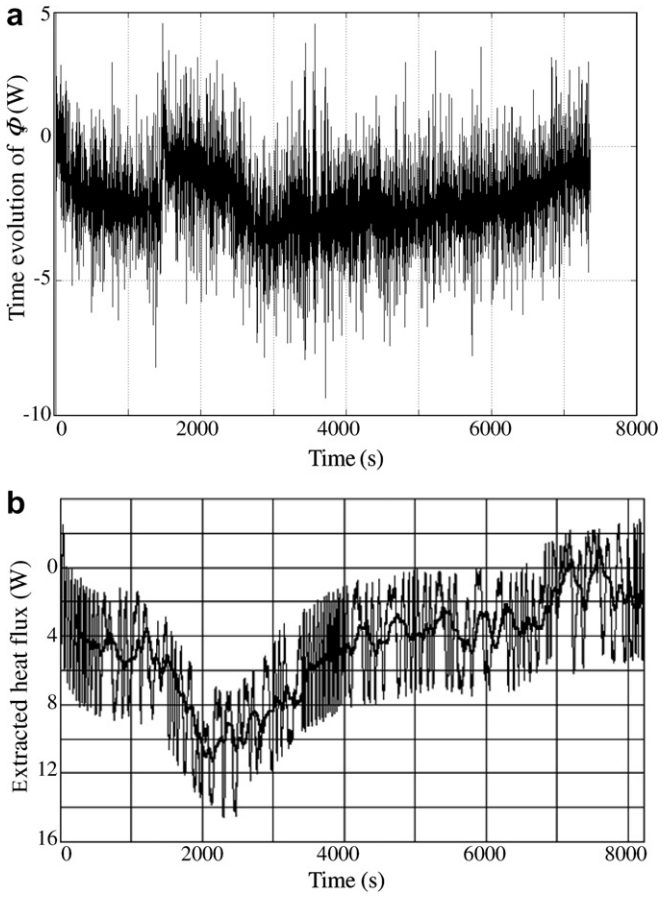

Fig. 10. Heat flux measurements in the tin–bismuth alloy case; cooling rate -2 K min^{-1}: (a) time evolution of the total heat stored in the sample corresponding to Φ_s in Eq. (5), (b) extracted heat flux Φ measured from the thermocouple located in the cooling system versus time; same conditions as in Fig. 6, cooling rate: -2 K min^{-1}.

slightly more pronounced in the slowest cooling rate. If we assume that the flow pattern consists of a counter-clockwise recirculation as sketched in Fig. 11d (the orientation of the segregated channels confirms that assumption), then the segregation pattern is consistent with the "washing effect" produced by the fluid flow inside the mushy zone. Indeed the liquid motion penetrates into the mushy zone and transports the solute from the mushy zone of the ingot towards the bottom part of the liquid pool. The segregations are localised in the zone where the assumed flow goes out of the mushy region. Then the bismuth accumulates in the bottom of the ingot which is solidified in the last stage of the process and also because of its high density.

4.3. Bismuth distribution

To obtain more quantitative information regarding the segregations, one ingot was cut by electro-erosion into a 12×10 element grid. We thus obtained 120 elements measuring $5 \times 5 \times 10$ mm. The bismuth in each element was proportioned by dissolution of the tin. The chart of the average bismuth concentration in each element is shown in Fig. 12. The accuracy of the concentration values is less than ± 1 wt.%. The average of the experimental values of Fig. 12 is equal to 10.1 wt.%. Since the nominal concentration is 10 wt.%, the latter result indicates that the solute mass is well conserved. Because of the averaging effect of the method, the zones of localised segregations cannot be detected. However, the distributed macro-segregations are clearly visible. The segregations are located in the bottom right of the ingot in accordance with the X-ray photographs of Fig. 11. Note firstly that the maximum concentration difference is quite high, i.e. from 6.7 wt.% to 19.6 wt.%. The location of the minimum and maximum values is very close. No satisfactory explanation has been found. However, it may be noticed that the segregation patterns exhibit the same overall tendency, but they are not exactly reproducible (in opposition to the temperature distribution). This is visible for example in Fig. 11a and b (or Fig. 11c and d) which correspond to the same experimental conditions.

4.4. Macrostructures

The macrostructures are very difficult to detect owing to the fact that tin is a soft metal which tends to spread out during polishing, thereby masking the structures. Moreover, the small dimensions of the sample make uniform polishing of the faces even more difficult. Consequently only two macrostructure analyses were carried out, on sample number 5 (cf. Fig. 13), one on the vertical face in contact with the thermocouples (Fig. 13a) and a second on a median vertical section (Fig. 13b).

The external map shows the development of long column-like grains with however smaller grains in the lower

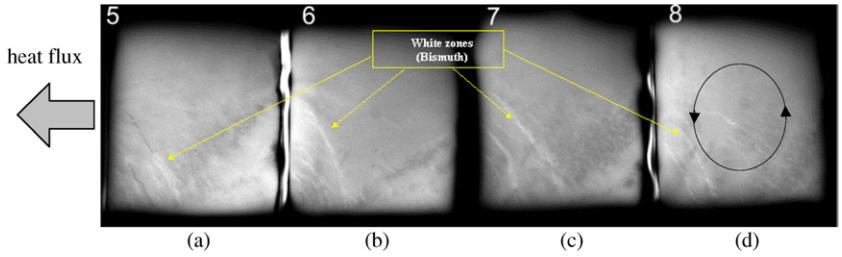

Fig. 11. Post-mortem patterns of the bismuth segregations (white zones) obtained from X-rays for two solidification speeds, namely -2 K min^{-1} for (a) and (b) and -5 K min^{-1} for (c) and (d); the assumed flow pattern is sketched in (d).

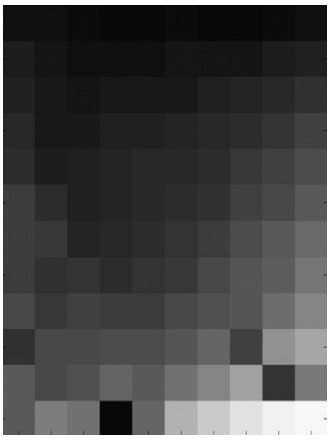

7.75	7.67	7.42	7.30	7.24	7.44	7.33	7.36	7.49	7.64
8.20	7.89	7.74	7.58	7.71	7.84	7.87	7.96	8.26	8.53
8.43	8.04	7.95	7.98	8.04	8.16	8.45	8.61	8.89	9.20
8.78	8.12	8.13	8.44	8.52	8.65	8.79	9.10	9.47	**10.00**
9.04	8.31	8.47	8.59	8.81	8.90	9.14	9.62	**10.08**	**10.67**
9.82	8.98	8.46	8.71	8.83	9.00	9.32	9.99	**10.51**	**11.34**
9.88	9.64	8.73	8.85	9.10	9.46	9.88	10.61	**11.23**	**12.10**
9.82	9.37	9.41	9.03	9.46	9.77	**10.39**	**11.09**	**11.39**	**12.79**
10.39	9.67	**10.01**	9.82	9.88	**10.44**	**10.91**	**11.09**	**12.32**	**13.45**
9.21	**10.53**	**10.49**	**10.76**	**10.63**	**11.03**	**11.88**	9.99	**14.13**	**15.15**
11.34	**10.58**	**10.91**	**11.91**	**11.25**	**12.47**	**13.52**	**14.81**	9.50	**12.96**
11.37	**13.05**	**12.43**	6.76	**11.90**	**15.68**	**16.98**	**18.06**	**18.96**	**19.63**

Fig. 12. Bi concentration map (left) and corresponding numerical values (right), $C_{min} = 6.76\%$; $C_{max} = 19.63\%$, sample no. 6 of Fig. 11, cooling rate: -2 K min^{-1}; positive segregations are indicated in bold characters.

right quarter that could correspond to equiaxed grains. Indeed, at the end of solidification the temperature gradient in the lower right quarter decreases because of the adiabatic conditions along the right lateral wall. Those thermal conditions are favorable for the triggering of a columnar-to-equiaxed transition. The second map shows some column-like grains, but a much greater quantity of small equiaxed grains. The black oblique traces, located

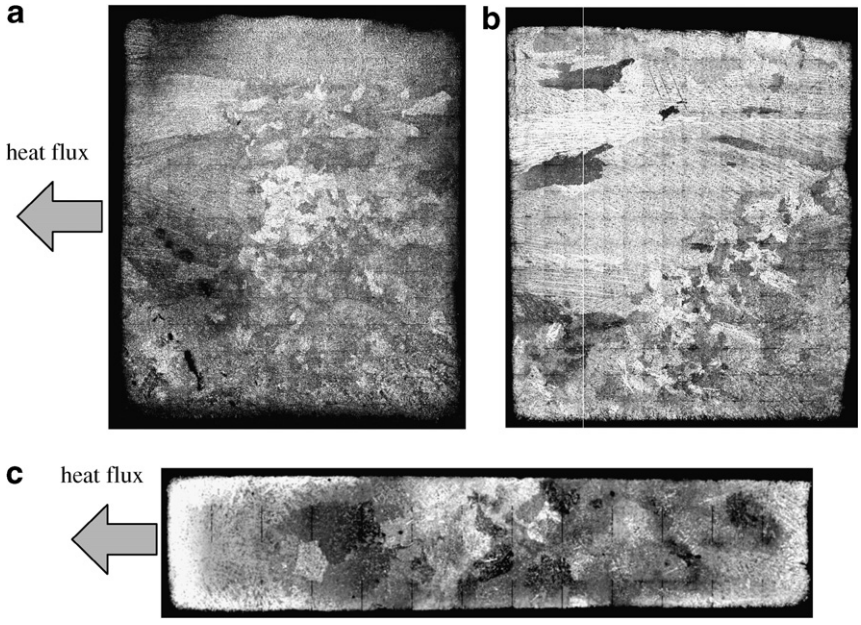

Fig. 13. Macrostructures: (a) mid-cross section of sample no. 5 of Fig. 11; (b) outer vertical side of the sample no. 5 of Fig. 11, cooling rate: -2 K min^{-1}; (c) macrostructure of sample no. 7 of Fig. 11, mid-horizontal plane, cooling rate: -5 K min^{-1}.

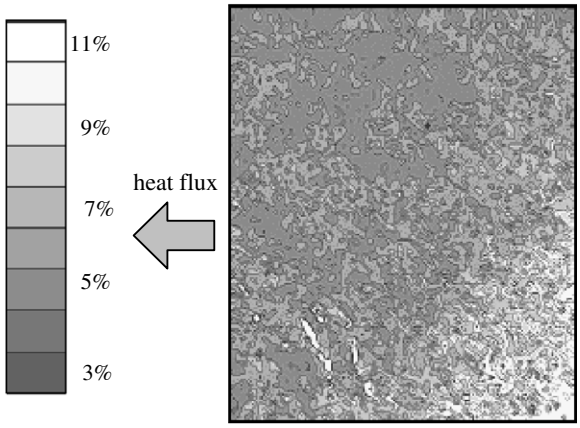

Fig. 14. Eutectic fraction map for the meridian section of sample no. 5 of Fig. 11; cooling rate: -2 K min^{-1}.

in the left lower quarter, correspond to zones of shrinkage pipes. They are in the development area of the segregated channels, as revealed by X-rays of the samples.

The eutectic fraction (Fig. 14) was mapped on the meridian face corresponding to ingot no. 5 of Fig. 11. This map represents the quantity of solid at the eutectic composition, the last to be solidified. The eutectic fraction may reach 11% for the richest zones. These rich zones correspond both to the segregated channels and to the final triangle of solidification (bottom right). The results obtained are in very good qualitative agreement with those obtained by X-ray analysis. Moreover, this chart once again confirms the existence of segregated channels.

5. Discussion and conclusions

The present experiment has shown that observed temperature maps as well as the segregations patterns were physically consistent. There are nevertheless some unexpected features. First, for the pure tin case, we observe an inversion of the bending of the solidification front. In the early stage of solidification (e.g. $t = 800$ s) the front curvature is consistent with the existence of counter-clockwise liquid convection which implies a downward liquid motion along the front and, accordingly, a slowing of front progression along its upper part. Furthermore, temperature fluctuations are still observable below the eutectic temperature, what makes the interpretation difficult.

We have observed that the temperature fluctuation level is much greater for the tin alloy case. The differences between the two cases can be interpreted in terms of differences in natural convection. In the alloy case, convection is created by both solutal and thermal buoyancy. Since bismuth is denser than tin, the solute rejection ahead of the solidification front leads to a downward motion. This solutal convection acts in the same way as thermal convection in the present situation. Moreover, the contribution of solute to buoyancy forces may be significantly greater than that coming from the temperature gradients. This is confirmed by the value of the buoyancy number N, which is a measure of the ratio between solutal and thermal buoyancy. Indeed, the dimensionless parameter N may be defined as follows [14]:

$$N = \frac{\beta_C \Delta C}{\beta_T \Delta T}, \tag{7}$$

ΔC and ΔT respectively being orders of magnitude of concentration and temperature differences. If we consider for example the mushy zone, ΔC and ΔT are related approximately by the thermodynamic equilibrium, and N can be expressed as [14]:

$$N = \frac{\beta_C}{m_L \beta_T}, \tag{8}$$

m_L being the liquidus slope in the phase diagram (see Appendix A).

Its numerical value $N = 19.5$ confirms that convection in the mushy zone is mainly of solutal type. It is then likely that natural convection is significantly more important than in the case of pure tin. Let us now estimate the velocity generated by natural convection in the liquid bulk. When the Grashof number is high (Eq. (10)), the estimate of the fluid velocity may be obtained from the balance between inertia and buoyancy, namely

$$U = \left(g \frac{\Delta \rho}{\rho} H \right)^{1/2}, \quad \text{with } \frac{\Delta \rho}{\rho} = \beta_T \Delta T + \beta_C \Delta C. \tag{9}$$

For the pure tin case, natural convection is driven by the temperature difference alone. An estimate of ΔT may be obtained from Fig. 4a at the onset of the solidification for example. The pool temperature difference is of order of 3 K. Then from (9), the estimated velocity is 1.4 cm/s. Concerning the order of magnitude of ΔC in the liquid bulk, its determination is not straightforward. For the case of the tin–bismuth alloy, the typical value of ΔC has been estimated by taking the root-mean-square value of the concentration deviation from the nominal concentration calculated from the values of Fig. 12. The typical concentration deviation is equal to 2.4 wt.%. The corresponding value of U is 6.6 cm s^{-1}. The latter value confirms the importance of solutal convection. The estimate of the corresponding Grashof number may be obtained from (9) as follows:

$$Gr = \left(\frac{UH}{\nu} \right)^2 = 1.94 \times 10^8. \tag{10}$$

That relatively high value confirms that the fluid inertia is globally dominant with respect to viscous forces, and the estimate (9) is relevant. It also indicates that the flow regime is no longer laminar.

Note that the turn-over time τ of the flow, estimated by

$$\tau = \frac{H}{U},$$

is equal to 0.9 s. The value of τ is very close to the peak frequency (0.8 Hz) of the temperature fluctuations measured by Quillet [13].

Concerning the macro-segregations, the pattern is in accordance with the observations of Hebditch and Hunt [11]. The experimental results have also been confirmed by numerical modeling of the present configurations (see for example [13]). Such a segregation pattern is created by a counter-rotating convection loop, which transports the solute towards the right bottom part of the ingot. Quillet has also shown numerically that the bottom right part of the ingot is the last zone to be solidified. This is consistent with the existence of a significant eutectic fraction in that part of the ingot.

Appendix A. Physical properties of tin and tin–wt10%bismuth alloy

The present appendix provides some physical properties of the alloy (Table A.1) as well as the phase diagram (Fig. A.1) obtained from [15].

Appendix B. Instantaneous temperature matrices for the pure tin case

The values of the recorded instantaneous temperature matrices for various times are given below. The representation is identical to that of Fig. 2. The temperature matrices are illustrated in Fig. 4

$$t = 800\ \text{s}: \begin{bmatrix} 234.65 & 235.61 & 236.27 & 236.88 & 237.03 \\ 234.49 & 235.80 & 236.41 & 236.59 & 237.93 \\ 234.49 & 235.86 & 236.41 & 236.47 & 236.83 \\ 234.43 & 235.55 & 236.20 & 236.51 & 236.51 \\ 234.29 & 235.34 & 235.45 & 236.15 & 236.21 \end{bmatrix} \quad \text{(B.1)}$$

Table A.1
Physical properties of pure tin and tin–wt.10%bismuth [15,16]

Physical properties of Sn–10%wtBi	Units	Values
Density at the melting point (alloy)	kg m^{-3}	6950
Thermal conductivity at the melting point (pure liquid tin)	W (m K)^{-1}	60
Kinematic viscosity (pure tin)	$\text{m}^2\,\text{s}^{-1}$	2.5×10^{-7}
Prandtl number (pure tin)		0.008
Schmidt number (pure tin)		136
Heat capacity at the melting point (pure liquid tin)	J (kg K)^{-1}	250
Latent heat (pure tin)	J kg^{-1}	60×10^3
Thermal expansion coefficient (pure tin)	K^{-1}	9.5×10^{-5}
Solutal expansion coefficient (pure tin)	$\text{wt.\%}^{-1}$	-3×10^{-3}
Partition coefficient (alloy)	–	0.37
Melting temperature (pure tin)	°C	231.9
Eutectic temperature (alloy)	°C	139
Liquidus temperature for the nominal concentration C_0 (alloy)	°C	215.8
Eutectic concentration (alloy)	wt.%	57
Liquidus slope (alloy)	$\text{K (\% wt)}^{-1}$	−1.62
Solute diffusion coefficient (pure tin)	$\text{m}^2\,\text{s}^{-1}$	1.8×10^{-9}

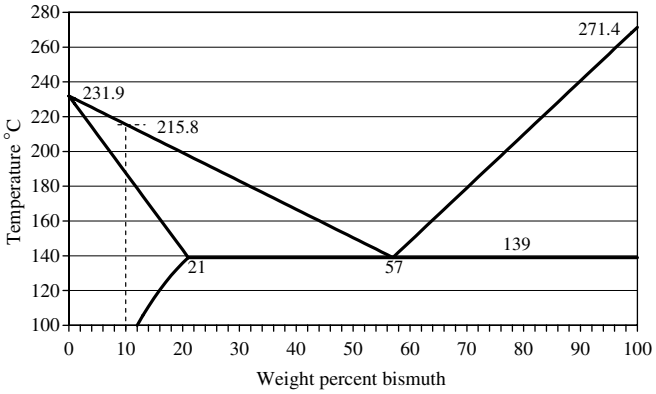

Fig. A.1. Phase diagram of the tin–bismuth alloy from [15].

$$t = 1000\ \text{s}: \begin{bmatrix} 231.19 & 232.45 & 233.06 & 233,58 & 233,39 \\ 231.88 & 233.31 & 233.75 & 233.84 & 233.93 \\ 232.34 & 233.96 & 234.49 & 234.36 & 234.27 \\ 232.91 & 234.33 & 234.84 & 234.75 & 234.55 \\ 233.21 & 234.76 & 234.19 & 234.92 & 234.67 \end{bmatrix} \quad \text{(B.2)}$$

$$t = 1250\ \text{s}: \begin{bmatrix} 227.92 & 230.42 & 231.43 & 232.30 & 231.91 \\ 228.85 & 231.89 & 232.75 & 232.93 & 232.93 \\ 229.40 & 232.83 & 233.95 & 233.94 & 233.71 \\ 229.94 & 233.15 & 234,51 & 234.62 & 234.33 \\ 229.74 & 233.16 & 233.49 & 234.84 & 234.67 \end{bmatrix} \quad \text{(B.3)}$$

$$t = 1750\ \text{s}: \begin{bmatrix} 221.34 & 225.79 & 228.06 & 229.68 & 229.28 \\ 222.61 & 227.68 & 229.99 & 231.05 & 231.18 \\ 223.24 & 228.18 & 231.02 & 232.37 & 232.38 \\ 223.55 & 227.93 & 230.95 & 232.67 & 233.03 \\ 222.96 & 227.65 & 229.38 & 232.51 & 233.30 \end{bmatrix} \quad \text{(B.4)}$$

Appendix C. Instantaneous temperature matrices for the tin–bismuth case

The recorded values of the instantaneous temperatures are given in the following matrices. Two cooling rates are considered. The temperature matrices are illustrated in Figs. 8 and 9.

Temperature distribution for 2 K min^{-1}

$$t = 1750\ \text{s}: \begin{bmatrix} 210.68 & 211.25 & 212.76 & 213.59 & 213.76 \\ 208.78 & 210.12 & 211.94 & 212.45 & 213.07 \\ 207.08 & 208.95 & 211.00 & 211.71 & 212.35 \\ 205.99 & 208.08 & 210,26 & 211.22 & 211.63 \\ 205.35 & 207.60 & 211.36 & 210.87 & 211.32 \end{bmatrix} \quad \text{(C.1)}$$

$$t = 2500\ \text{s}: \begin{bmatrix} 195.06 & 197.06 & 200.58 & 204.08 & 206.18 \\ 193.87 & 195.83 & 199.08 & 202.59 & 205.15 \\ 192.55 & 194.65 & 198.01 & 201.41 & 204.09 \\ 190.69 & 193.53 & 197.37 & 200.66 & 202,24 \\ 189.04 & 192.87 & 199.97 & 199.97 & 201,87 \end{bmatrix} \quad \text{(C.2)}$$

Temperature distribution for 5 K min^{-1}

$$t = 640\ \text{s}: \begin{bmatrix} 211.44 & 213.50 & 215.02 & 215.38 & 215.39 \\ 208.87 & 212.42 & 215.03 & 215.09 & 215.39 \\ 206.66 & 211.28 & 214.76 & 214.95 & 215.08 \\ 205.35 & 210.16 & 214.05 & 214.86 & 214.77 \\ 205.37 & 209.61 & 213.10 & 214.25 & 214.31 \end{bmatrix} \quad \text{(C.3)}$$

$$t = 840\ \text{s}: \begin{bmatrix} 198.50 & 202.43 & 208.46 & 213.19 & 215.14 \\ 195.57 & 201.10 & 207.56 & 212.44 & 215.07 \\ 192.99 & 199.42 & 206.21 & 211.21 & 214.28 \\ 191.60 & 198.07 & 204.90 & 210.20 & 212.69 \\ 191.32 & 197.67 & 204.44 & 209.07 & 210.88 \end{bmatrix} \quad \text{(C.4)}$$

References

[1] A.F. Giamei, B.H. Kear, On the nature of freckles in nickel base superalloys, Metall. Trans. 1 (1970) 2185–2192.

[2] A. Hultgren, A and V segregation in killed steel ingots, Scand. J. Metall. 2 (1973) 217–227.

[3] L.H. Shaw, J. Beech, R.H. Hickley, Channel segregates in cast steel rolls, Ironmaking and Steelmaking 13 (1986) 154–160.

[4] T.M. Pollock, W.H. Murphy, The breakdown of single-crystal solidification in high refractory nickel-base alloys, Metall. Mater. Trans. A 27 (1996) 1081–1094.

[5] P. Auburtin, S.L. Cockroft, A. Mitchell, Liquid density inversions during the solidification of superalloys and their relation ship to freckle formation in castings, in: J. Beech, H. Jones (Eds.), Solidification Processing 1997, The University of Sheffield (GB), 1997, pp. 336–340.

[6] R.J. McDonald, J.D. Hunt, Fluid motion through the partially solid regions of a casting and its importance in understanding A-type of segregation, Trans. Metall. Soc. AIME 245 (1969) 1993–1997.

[7] J.R. Sarazin, A. Hellawell, Channel formation in Pb–Sn, Pb–Sb, and Pb–Sn alloy ingots and comparison with the system NH_4Cl–H_2O, Metall. Trans. A 19 (1988) 1861–1871.

[8] N. Streat, F. Weinberg, Macrosegregation during solidification resulting from density differences in the liquid, Metall. Trans. 5 (1974) 2539–2548.

[9] S.N. Tewari, R. Shah, Macrosegregation during steady-state arrayed growth of dendrites in directionnaly solidified Pb–Sn alloys, Metall. Trans. A 23 (1992) 3383–3392.

[10] C. Gau, R. Viskanta, Melting and solidification of a pure metal on a vertical wall, J. Heat Trans. – T. ASME 108 (1986) 174–181.

[11] D.J. Hebditch, J.D. Hunt, Observations of ingot macrosegregation on model systems, Metall. Trans. 5 (1974) 1557–1564.

[12] M.I. Bergman, D.R. Fearn, J. Bloxham, M.C. Shannon, Convection and channel formation in solidifying Pb–Sn alloys, Metall. Mater. Trans. A 28 (1997) 859–866.

[13] G. Quillet, Influence de la convection, naturelle ou forcée, sur l'apparition des mésoségrégations lors de la solidification des alliages métalliques, Ph.D. thesis, INP Grenoble, 2003.

[14] P.J. Prescott, F.P. Incropera, The effect of turbulence on solidification of a binary metal alloy with electromagnetic stirring, J. Heat Transfer 117 (1995) 716–724.

[15] T.B. Massalski, in: William W. ScottJr. (Ed.), Binary Alloy Phase Diagrams, vol. 1, The American Society for Metals, 1986.

[16] E.A. Brandes, G.B. Brook, Smithell Metals Reference Book, 7th ed., Butterworth-Heineman, Oxford, UK, 1992.